



UiT The Arctic University of Norway

Faculty of Science and Technology, Department of Physics and Technology

Semi-automatic estimation of mandibular cortical width in dental panoramic radiographs for early osteoporosis detection

Isak Paasche Edvardsen

STA-3740, Spring 2021



Contents

1	Introduction	8
2	Diagnosis	8
2.1	Mandibular cortical width	9
2.2	Klemetti index	9
2.3	Disadvantages of panoramic radiographs	11
3	Theory	12
3.1	Pre-processing	12
3.1.1	Region extraction	12
3.1.2	Normalization and standardization	13
3.2	Image processing	14
3.2.1	Histograms and intensities	14
3.2.2	Histogram equalization	14
3.2.3	Smoothing	14
3.2.4	Global Otsu	16
3.2.5	Laplacian of a Gaussian	18
3.2.6	Ridge detection	19
3.2.7	Hough transform	19
4	Experiments	21
4.1	Identify the mental foramen	22
4.2	Measuring the bone	26
4.3	Results and discussion	33
4.4	Classification?	36
5	Concluding remarks	36
5.1	Future work	36
5.2	Appendix	37

Acknowledgments

I want to thank my advisers, Fred Godtliebsen, Thomas Haugland Johansen, Jonas Nordhaug Myhre, Anna Teterina, and Napat Limchaichana Bolstad. With their effort and feedback, this project was a pleasant experience. Furthermore, I want to thank my family and friends for their encouragement throughout another peculiar semester.

Anatomical structure found on panoramic radiographs

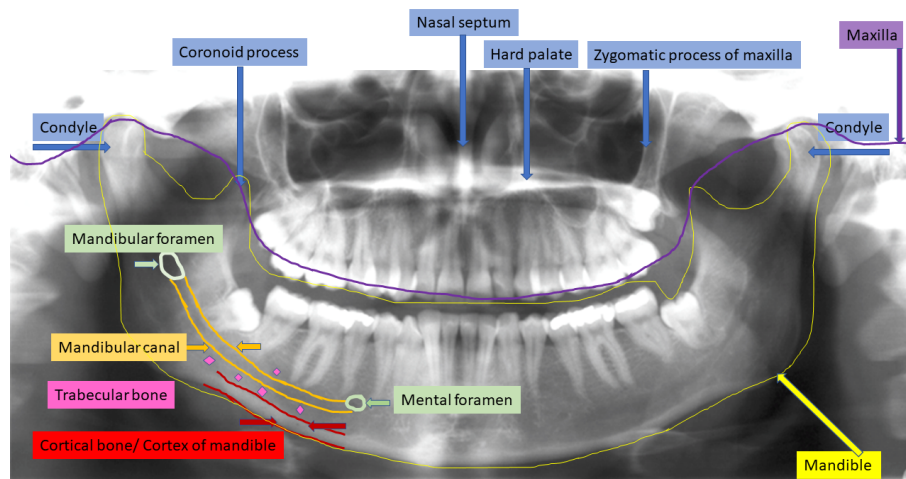


Figure 1: The figure shows important structures such as the mental foramen and cortical bone.

List of Figures

1	The figure shows important structures such as the mental foramen and cortical bone.	5
2	The figure demonstrates how to measure the mandibular cortical width.	9
3	The figure shows three cases of classifying bone erosion by the Klemetti index.	10
4	The figure displays how the region of interest is placed on every panoramic radiograph.	13
5	Image (a) shows the ROI, image (b) shows (a) smoothed with a Gaussian filter with kernel size 7, and (c) shows histogram equalization applied to (b).	15
6	The figure illustrates how a threshold obtained by Otsu's method can produce a binary mask.	18
7	kan man bruke denne?	21
8	Figure column (a) displays the original low contrast image, and column (b) displays the image after the contrast has been stretched to fill the intensity range. Column (c) displays the contrast stretched as proposed.	21
9	Figure column (a) shows the ROI, column (b) shows (a) after histogram equalization, column (c) shows (b) after gray-scale erosion.	22
10	Figure column (c) the shows the gray-scale eroded image, then we see the histogram with three obtain thresholds. Far-right, the thresholded image is observed.	23
11	Figure column (d) shows the binary image obtained from threshold two, column (e) shows the (d) inverted, column (f) shows (d) after regions meeting the border has been removed.	23
12	The figure shows the resulting contour and bounding box around the smallest region from figure 11f.	24
13	The figure presents two situations where the proposed method disappoints.	24
14	Image (a) shows the ROI, image (b) shows (a) after a median filter is applied, and image (c) shows a binary mask obtained from Otsu's method, image (d) shows image (b) multiplied with (c), image (e) shows (d) inverted, exposing the MF, image (f) shows the output after blob detection.	25
15	Image (a) displays the ROI, image (b) shows the variance image obtained after (a) is filtered with a median filter, image (c) shows (b) after histogram equalization, and image (d) shows the binary image I_b	27
16	Figure column (a) shows an image and the resulting binary image of a Klemmti index C1, in the same manner (b) shows a case of C2, and column (c) displays a state of C3.	28

17	Image (a) displays the median filtered ROI, image (b) shows the result of gray-scale dilation applied to the variance image of (a), (c) presents the binary image with thee thresholds, image (d) shows the contour of the candidate region after region labeling. .	29
18	Here we see the input line, which is a part of the lowest contour of the candidate region, and the resulting lines after classical Hough transform.	30
19	The figure displays an example of the initial and final state of the scheme.	30
20	The figure displays both the initial and final line from which we measure the mandibular cortical width.	31
21	Figure image (a) displays ROI exposed to a Gaussian blur with kernel size 5, image (b) shows the Frangi filter response of image (a), image (c) shows the HHF response of image (a).	32
22	Figure image (a) displays a binary mask after a closing operation is applied to figure (21c), image (b) shows the most prominent contour and associated bounding box found in the image (a), image (c) shows a binary mask of the region bounded by the contour.	32
23	Image (a) shows a suitable line overlapping the binary mask, whereas (b) shows the same composition in the non-binary setting.	33

1 Introduction

Processing digital images is critical for detecting, examining, and assisting specialists in determining a patient's condition, disease, or illness. Different processing techniques are used in different fields, whether they are used to process image data or improve images for human interpretation. The latter is frequently used in clinical settings, including dentistry. Since the mineral content of the cortical bone of the mandible is thought to be correlated with that of the skeleton, routine panoramic radiographs of the mouth can provide important information to use in identifying those at risk for osteoporosis [1, 2]. A number of measures, such as the mandibular cortical width (MCW), the panoramic mandibular index (PMI), and the mandibular ratio (M/M), have been designed to evaluate jawbone mass and observe signs of resorption. Throughout this paper, we will focus on the MCW. Essentially, osteoporosis is a condition in which bones become fragile due to a loss of bone mass, leading to pain, fractures, disability, and a greater inability to perform daily activities. Osteoporosis is not only a considerable cause of fractures; it also ranks highly among diseases that can render individuals bedridden with serious complications [3]. Elderly individuals may be at risk of life-threatening complications from these conditions [4]. Early detection of osteoporosis may thus reduce the risk of fractures and improve the quality of life for many individuals.

2 Diagnosis

In accordance with the WHO criteria, osteoporosis is defined as a bone mineral density (BMD) that is 2.5 standard deviations or more below that of a average, young, healthy women (a T-score of < -2.5 SD) [4]. BMD is most commonly assessed by dual-energy X-ray absorption (DXA), which is the most widely validated method. The primary problem with the sole use of BMD tests is that DXA is not readily available and is commonly used for research purposes because of its high capital costs.

Studies suggest that routine dental radiographs could be an important tool for identifying individuals at risk for osteoporosis and refer them for bone mineral density testing. On the basis of dental radiographs, there are several significant predictors of mandibular stability. Among these are the mandibular cortical width proposed by Horner and Devlin [5], the panoramic mandibular index (PMI) presented by Benson et al. [6], and the Klemetti index [7].

2.1 Mandibular cortical width

The mandibular cortical width (MCW) is defined as the measurement of the cortical thickness of the mandible taken below the mental foramen (figure 2). Several studies [8, 9, 10, 11, 12] have shown that MCW, as measured on dental panoramic radiographs, can help identify postmenopausal women with low bone mineral density or osteoporosis. Therefore, dentists can differentiate osteoporosis suspects based on minor findings on dental panoramic radiographs without the additional cost of DEXA and refer them for BMD analysis. Yet, it is not ideal to measure cortical width on dental panoramic radiographs to identify individuals with low skeletal mass, due to the bone's unclear borders, which can lead to varying measurements between dentists.



Figure 2: The figure demonstrates how to measure the mandibular cortical width.

2.2 Klemetti index

As mentioned, the klemmeti index [7] is also used for establishing low BMD by classifying bone erosion in three groups by the following criteria:

C1: Normal cortex, even and sharp endosteal¹ margin on the both sides

¹located within bone

C2: Mildly-to-moderately eroded cortex, some endosteal cortical residues (semilunar defects) on one or both sides.

C3: Severely eroded cortex, heavy endosteal cortical residues, cortex is clearly porous.

Taguchi et al. investigated whether the Klemetti index and mandibular cortical width could predict osteoporosis in postmenopausal Japanese women. The authors concluded that postmenopausal women with changes to the mandible may have an increased risk of low vertebral BMD or osteoporosis. Study participants with severely eroded cortex (C3) had a 14.0% greater likelihood of having vertebral osteoporosis, and participants with both thin cortical width and severely eroded cortex had a 23.0% greater probability [13]. This may suggest that the Klemetti index could assist in predicting osteoporosis.

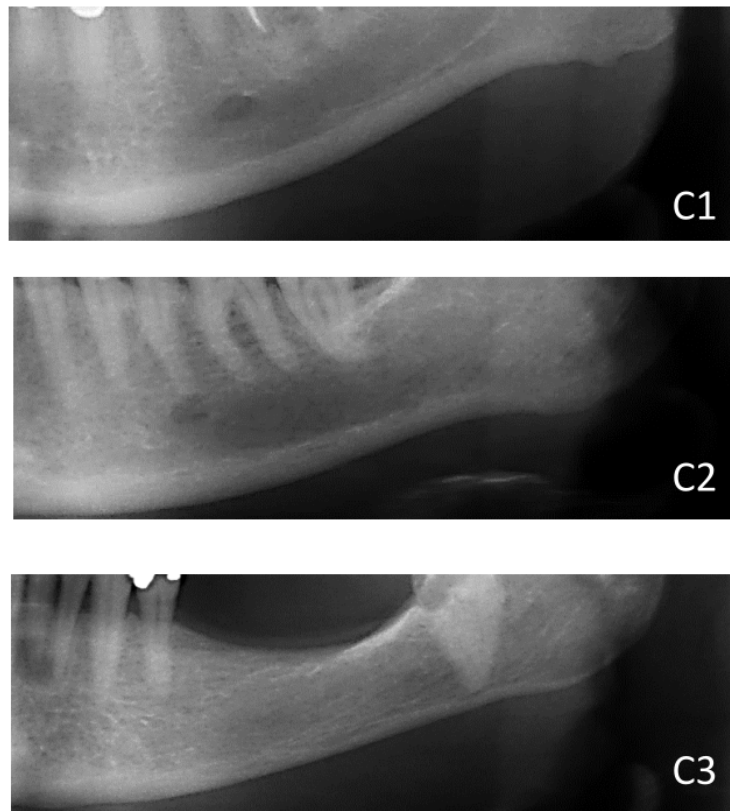


Figure 3: The figure shows three cases of classifying bone erosion by the Klemetti index.

2.3 Disadvantages of panoramic radiographs

Indeed panoramic radiographs are prudent, yet there are drawbacks. They are generally complex because of artificial structures, imprecise edges of skeletal structures, ghost images from the spine, jawbones with uneven curves and intensity levels, and unsuitable positioning of the patient.

If a patient is poorly positioned, it is difficult to determine the magnification rate, a consequence of panoramic radiography. The position of an object in relation to both the x-ray source and its receptor (film) determines the degree of magnification. Imagine a patient is positioned correctly within the panoramic unit and the object of interest is located within the focal area. We then determine the magnification rate from the panoramic machine manual (usually about 15-25%). As the x-ray beam passes around the patient's head, some anatomical structures are projected twice on the receptor, resulting in ghost images overlapping with critical anatomical structures. It is possible that the angle between the horizontal plane and the central x-ray beam will ascend during the exposure cycle, causing distortion in the object's shape and in spatial relationships between anatomical structures. All of these pitfalls need to be considered when interpreting panoramic radiographs, and linear measurements taken from panoramic radiographs need to be considered cautiously. As well, the mental foramen can have irregular shapes and unclear borders. Usually, the MF is located below the premolar tooth [14] (tooth five from front to back), but irregular tooth alignments or missing pieces make it more difficult to determine where the MF is located. It is most common for there to be only one MF [15], increasing the difficulty of detection.

3 Theory

All the image processing techniques discussed in this chapter are implemented in the spatial domain. Spatial filters are fundamental in image processing applications. Spatial filtering modifies an image by replacing each pixel value with a function of the pixel values and their neighbors. If the function is linear, the filter is called linear spatial filtering; otherwise, it is a nonlinear spatial filter. A linear spatial filter performs a sum-of-products operation between an image f and a filter kernel, w . The neighborhood of operation is defined by the kernel size, which is an array whose coefficients determine the filter's character [16]. The convolution of a kernel w of size $m \times n$ with an image $f(x, y)$, denoted $(w * f)(x, y)$, is defined as

$$(w * f)(x, y) = \sum_{s=-a}^a \sum_{t=-b}^b w(s, t) f(x - s, y - t) \quad (1)$$

3.1 Pre-processing

3.1.1 Region extraction

The mental foramen is one of two openings located on the anterior surface of the mandible (jawbone). However, the area around the mental foramen is suffered with low contrast and dark color. Hence we stretched the appropriate range of intensity values corresponding to the area of interest. Because the original panoramic radiographs had very high resolution, a region of interest was extracted for fast and straightforward computing. They were cropped manually on the right and left sides with assistance from two experts determining if the region was appropriate. The area (300×500 pixels) captures the lower border of the mandibular cortex below the mental foramen.

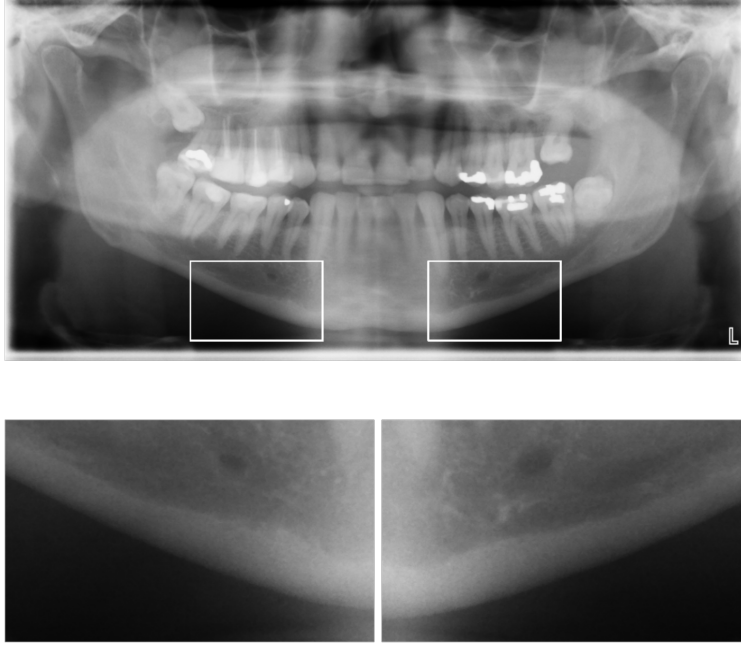


Figure 4: The figure displays how the region of interest is placed on every panoramic radiograph.

3.1.2 Normalization and standardization

As the radiographic images are 16-bit images, they can take on pixel values ranging from 0 to 2^{16} . However, they never span the entire range, making them cumbersome to work with while recognizing their bright or dark pixel values. Therefore normalization (2) is applied, addressing pixel values ranging from 0 to 1, meaning zero is darkest and one is brightest, which is more intuitive. Standardization (3) is also utilized so that the relative differences between the images are maintained. This process is practical when analyzing the statistic for an image, e.g., in texture analysis, where the variance is used.

$$z_i = \frac{x_i - \min(x)}{\max(x) - \min(x)} \quad (2)$$

where x_i is image i , $\min(x_i)$ is the minimum value of the image and $\max(x_i)$ is the maximum value of the image.

$$z = \frac{x - \mu}{\sigma} \quad (3)$$

where x is the data set, μ is the mean value of the data set and σ is the standard deviation of the data set.

3.2 Image processing

3.2.1 Histograms and intensities

Histogram manipulation and intensity transformations are fundamental tools in image processing. The latter is based on the expression $o(x, y) = T[i(x, y)]$, where $i(x, y)$ is the input image and $o(x, y)$ is the output image after the operator T is applied on the input over a neighborhood of points (x, y) or the whole image. We will later see the negative of an image with intensity levels in the range $[0, L - 1]$, acquired using the negative transformation function $s = L - 1 - r$. Here r denotes input intensity levels and s output intensity levels.

3.2.2 Histogram equalization

Histogram equalization is a technique for adjusting image intensities to enhance contrast globally, mainly when close contrast values represent the valuable data of the image. The method is adequate in images with backgrounds and foregrounds that are both bright or dark.

Let f be a given image represented as an $m \times n$ matrix of integer pixel intensities on the range $r = [0, L - 1]$. L is the number of possible intensity values, in this case, 2^{16} . Let p denote the normalized image histogram of f with a bin for each possible intensity. So

$$p_n = \frac{\text{number of pixels with intensity } n}{MN} \quad n = 0, 1, \dots, L - 1.$$

where MN is the total number of pixels.

The histogram equalized image g will be defined by

$$g_{i,j} = \text{floor} \left((L - 1) \sum_{n=0}^{f_{i,j}} p_n \right) \quad (4)$$

where $\text{floor}()$ rounds down to the nearest integer. This is equivalent to transforming the pixel intensities k , of f by the function

$$T(k) = \text{floor} \left((L - 1) \sum_{n=0}^k p_n \right) \quad k = 0, 1, 2, \dots, L - 1. \quad (5)$$

3.2.3 Smoothing

Smoothing (or averaging) spatial filters are commonly used to reduce sharp transitions in intensity. There are numerous applications where smoothing is appropriate, such as reducing noise, reducing aliasing, and blurring false contours. Smoothing is also a method to reduce unnecessary detail in an image, where "unnecessary" refers to small pixel regions compared to the filter's kernel size. Smoothing filters can additionally be used in combination with other techniques.

Gaussian kernels are an attractive choice because of their circular symmetry (isotropic), and they are separable. Meaning the Gaussian blur can be applied to a two-dimensional image as two independent one-dimensional calculations.

In two dimensions the formula for a Gaussian function is the product of two, one in each dimension

$$w(s, t) = G(s, t) = K e^{-\frac{s^2+t^2}{2\sigma^2}} \quad (6)$$

$$\text{where } K = \frac{1}{2\pi\sigma^2} \quad (7)$$

By letting $r = [s^2 + t^2]^{1/2}$ we can rewrite the above expression as

$$G(r) = K e^{-\frac{r^2}{2\sigma^2}}$$

where variable r is the distance from the center to any point on function G .

Another smoothing filter is the median filter; it is in the class of nonlinear spatial filters whose response is based on ordering the pixels in the area contained by the filter. The median filter replaces the center pixel's value with the median of the intensity values in the neighborhood of that center pixel. This filter is probably the most famous for its effectiveness in the presence of salt-and-pepper noise. The median \tilde{x} , of a set of values is such that half the values in the set are less than or equal to \tilde{x} , and half are greater than or equal to \tilde{x} [16]. Essentially the midpoint in a list of ordered values. In a 3×3 neighborhood the median is the 5th largest value.

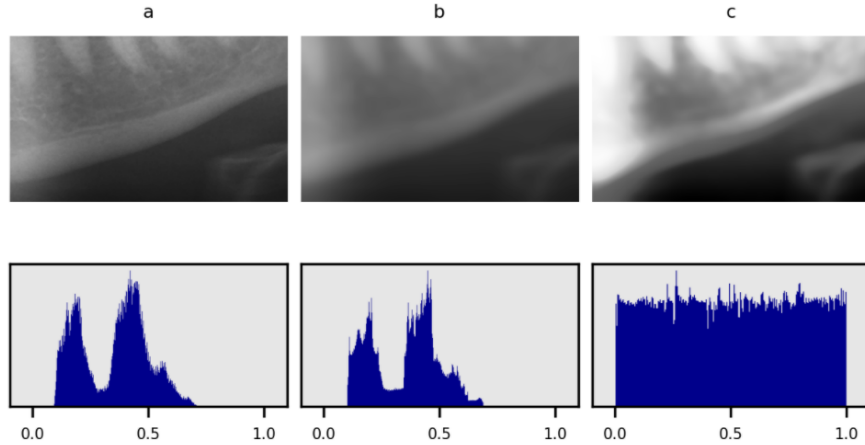


Figure 5: Image (a) shows the ROI, image (b) shows (a) smoothed with a Gaussian filter with kernel size 7, and (c) shows histogram equalization applied to (b).

3.2.4 Global Otsu

Otsu's method is used to achieve automatic image thresholding; in the simplest case, it partitions the image into two classes, foreground, and background. The method is optimum because it maximizes the between-class (intensity) variance, or equivalently, minimizing intra-class variances, defined as a weighted sum of the classes' variances. Otsu's method is a one-dimensional discrete analog of Fisher's discriminant analysis since it is performed on the 1-D histogram array. The principle is that the pixels' intensity values between classes should be distinct for a properly thresholded image; a threshold resulting in the best partition between classes in terms of their intensity values would be optimum [16].

The method works as follows; compute the normalized histogram, which has components $p_i = n_i/MN$ for an image represented as a $m \times n$ matrix, where n_i denotes the number of pixels with intensity i , from which it follows that

$$\sum_{i=0}^{L-1} p_i = 1 \quad p_i \geq 0$$

If we select a threshold $T(k) = k$, $0 < k < L - 1$, and use it to separate an image into two classes, c_1 and c_2 , with respect to the pixel intensities

$$g(x, y) = \begin{cases} c_1, & \text{for pixels in range } [0, k] \\ c_2, & \text{for pixels in range } [k + 1, L - 1] \end{cases}$$

Then the probability that a pixel is assigned to class c_1 is given by the cumulative sum

$$P_1(k) = \sum_{i=0}^k p_i \tag{8}$$

similarly, for class c_2 occurring

$$P_2(k) = \sum_{i=k+1}^{L-1} p_i = 1 - P_1(k) \tag{9}$$

Following, the mean intensity value of a pixel in c_1 is

$$\begin{aligned} m_1(k) &= \sum_{i=0}^k iP(i/c_1) \stackrel{Bayes'}{=} \sum_{i=0}^k iP(c_1/i)P(i)/P(c_1) \\ &= \frac{1}{P_1(k)} \sum_{i=0}^k ip_i \end{aligned} \tag{10}$$

the mean intensity value of the pixel assigned to c_2 is, similarly

$$m_2(k) = \sum_{i=k+1}^{L-1} iP(i/c_2) \quad (11)$$

$$= \frac{1}{P_2(k)} \sum_{i=k+1}^{L-1} ip_i \quad (12)$$

The cumulative mean up to level k is given by

$$m(k) = \sum_{i=0}^k ip_i \quad (13)$$

The global mean is given by

$$m_G = \sum_{i=0}^{L-1} ip_i \quad (14)$$

clearly, the probabilities must sum to one, which also leads to the following

$$P_1 + P_2 = 1 \quad (15)$$

$$P_1 m_1 + P_2 m_2 = m_G \quad (16)$$

We have omitted the k s tentatively in favor of notational simplicity.

To assess the effectiveness of the threshold about level k , we use the normalized, dimensionless measure

$$\nu = \frac{\sigma_B^2}{\sigma_G^2} \quad (17)$$

where σ_G^2 is the global variance

$$\sigma_G^2 = \sum_{i=0}^{L-1} (i - m_G)^2 p_i \quad (18)$$

and σ_B^2 is the *between-class variance*, defined as

$$\sigma_B^2 = P_1(m_1 - m_G)^2 + P_2(m_2 - m_G)^2 \quad (19)$$

$$= P_1 P_2 (m_1 - m_2)^2 \quad (20)$$

$$= \frac{(m_G P_1 - m)^2}{P_1(1 - P_2)} \quad (21)$$

From line (20), we perceive that the more significant gap between means m_1 and m_2 , the large σ_B^2 will be, implying that the between-class variance is a measure of separability between classes.

Reintroducing k , we get:

$$\nu(k) = \frac{\sigma_B^2(k)}{\sigma_G^2} \quad (22)$$

$$\text{and } \sigma_B^2(k) = \frac{[m_G P_1(k) - m(k)]^2}{P_1(k)[1 - P_2(k)]} \quad (23)$$

Then, the best threshold is the value, k^* , that maximizes $\sigma_B^2(k)$:

$$\sigma_B^2(k^*) = \max_{0 \leq k \leq L-1} \sigma_B^2(k)$$

one k^* is obtained, the input image is segmented as before

$$g(x, y) = \begin{cases} 1, & \text{if } f(x, y) > k^* \\ 0, & \text{if } f(x, y) \leq k^* \end{cases}$$

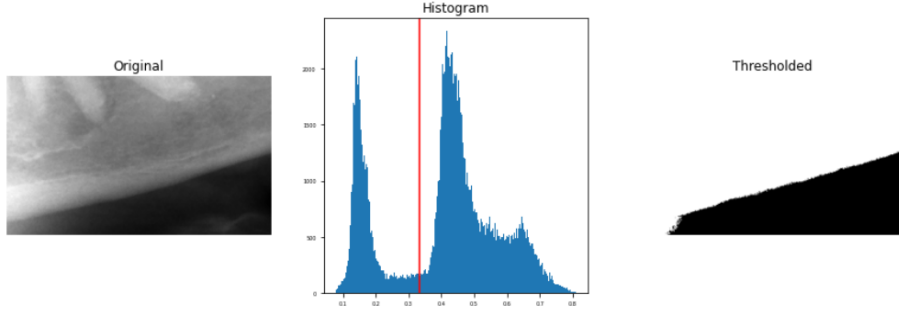


Figure 6: The figure illustrates how a threshold obtained by Otsu's method can produce a binary mask.

3.2.5 Laplacian of a Gaussian

Blod detection is a method that aims to detect regions in an image that differ in characteristics, such as intensity, size, shape, or color, compared to surrounding regions. For example, the mental foramen can be considered a blob. Unofficially, a blob is a region where attributes are constant, meaning every point within a blob is alike.

There are several methods to detect blobs; here, we will cover and later apply the Marr-Hildreth algorithm. The latter consists of convolving the Laplacian of a Gaussian (LoG) kernel with an input image [16]

$$g(x, y) = [\nabla^2 G(x, y)] * f(x, y) \quad (24)$$

we have already covered the Gaussian kernel G , but for now, we are only interested in the general shape

$$G(x, y) = e^{-\frac{x^2+y^2}{2\sigma^2}} \quad (25)$$

Applying the Laplacian we obtain an expression for $\nabla^2 G(x, y)$

$$\nabla^2 G(x, y) = \frac{\partial G(x, y)}{\partial x^2} + \frac{\partial G(x, y)}{\partial y^2} \quad (26)$$

$$= \frac{\partial}{\partial x} \left(\frac{-x}{\sigma^2} e^{-\frac{x^2+y^2}{2\sigma^2}} \right) + \frac{\partial}{\partial y} \left(\frac{-y}{\sigma^2} e^{-\frac{x^2+y^2}{2\sigma^2}} \right) \quad (27)$$

$$= \left(\frac{x^2}{\sigma^4} - \frac{1}{\sigma^2} \right) e^{-\frac{x^2+y^2}{2\sigma^2}} + \left(\frac{y^2}{\sigma^4} - \frac{1}{\sigma^2} \right) e^{-\frac{x^2+y^2}{2\sigma^2}} \quad (28)$$

$$= \left(\frac{x^2 + y^2 - 2\sigma^2}{\sigma^2} \right) e^{-\frac{x^2+y^2}{2\sigma^2}} \quad (29)$$

We have stated that the Gaussian operator blurs the image, reducing noise and intensities of structures at scales much smaller than σ . The Laplacian has the critical advantage of being isotropic, responding equally to changes in intensity in any kernel direction. This is a more attractive option over using first derivatives, which are directional operators requiring multiple kernels; see Sobel operators [17].

3.2.6 Ridge detection

Ridge detection is a valuable tool for obtaining ridge-like structures like vessels, wrinkles and rivers in an image. Note that a ridge is not the same as an edge; the boundary between two regions is an edge, while a ridge is a line lighter or darker than their neighborhood. Frangi et al. [18] introduced a filter for vessel extractions which is frequently applied for retinal vessel detection [19, 20]. Choon-Ching Ng et al. [21] have proposed a method for wrinkle detection, that is hybrid Hessian filter (HHF).

The concept behind such a filter is based on second-order partial derivatives, where the eigenvalues of the Hessian matrix are used to obtain the principal directions in which the local second-order structure of the image can be decomposed [22].

3.2.7 Hough transform

The classical Hough transform was concerned with recognizing lines in an image. Later the Hough transform has been extended to identifying arbitrary shapes. The technique aims to find objects within a distinct class of shapes by

a voting scheme. This voting scheme is carried out in parameter space. Object candidates are obtained as local maxima in an accumulator space assembled by the Hough transform algorithm. Assume we want to find subsets of points in an image with n points, which lie on straight lines. Instead of finding all lines determined by every pair of points and then finding all subsets of points near particular lines, Hough suggested an alternative approach, commonly referred to as the Hough transform. Let (x, y) denote a point in the xy-plane and consider the equation of a straight line

$$y_i = ax_i + b \quad (30)$$

Infinitely many lines pass through (x_i, y_i) , and for varying values of a and b , they all satisfy equation (30).

Writing this equation as:

$$b = -x_i a + y_i \quad (31)$$

and considering the ab -plane (parameter space) produces the equation of an individual line for a fixed point (x_i, y_i) . A second point (x_j, y_j) will also have a single line in parameter space associated with it, and it will intersect the line associated with (x_i, y_i) at some point (a', b') in parameter space, where a' and b' is the slope and the intercept, respectfully, of the line including both (x_i, y_i) and (x_j, y_j) in the xy-plane. All points on this line will have lines in parameter space that intersect at (a', b') .

The lines in parameter space corresponding to all points (x_k, y_k) in the xy-plane could be plotted. The main lines in the xy-plane could be determined by identifying points in the parameter space where numerous parameter-space lines intersect, hence the voting scheme. However, a challenge with this procedure is that the slope of the line can approach infinity. To overcome this problem, one can use the normal representation of a line:

$$x \cos \theta + y \sin \theta = \rho \quad (32)$$

Subdividing the parameter space into accumulator cells gives rise to the attractiveness of the Hough transform. Accumulator values $A(i, j)$ at cell (i, j) corresponds to the square associated with parameter values (θ_j, ρ_j) . For each foreground point (x_k, y_k) in the threshold image, we let θ_j equal all possible θ values and we solve for ρ using equation (32). Then we round ρ to the closest cell value, ρ_q , and increment $A(i, j)$ until the procedure is finished. A value of $A(i, j) = P$ means that P points in the xy-space lie on the line $\rho_j = x \cos \theta_j + y \sin \theta_j$. Hence the voting scheme.

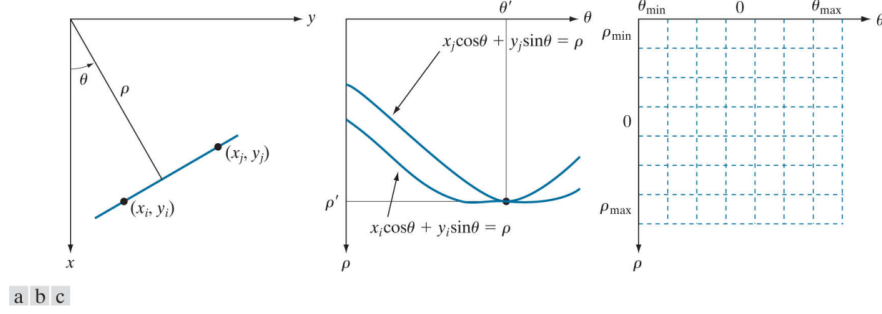


Figure 7: kan man bruke denne?

4 Experiments

The experiments in this section are concerned with two separate tasks. First, we will try to identify the mental foramen, as it is common practice to measure the bone below it. After, we will seek to measure the bone. Henceforward, the ROI is used, and the contrast is stretched, so it is within the 5% and 95% percentiles. Because pixels under 5% are considered background variation, above 95% are assigned as the teeth and ghost image from the spine. The latter can be a severe problem if illuminated.

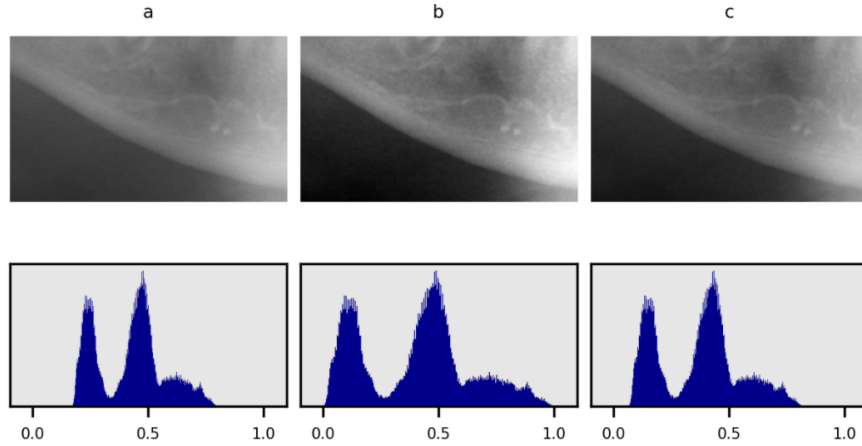


Figure 8: Figure column (a) displays the original low contrast image, and column (b) displays the image after the contrast has been stretched to fill the intensity range. Column (c) displays the contrast stretched as proposed.

4.1 Identify the mental foramen

Two methods have been tested for the identification. Up first, we have adapted the method proposed by Aliaga et al. [23]; second, we will try a different method using image enhancing techniques. Aliaga et al. suggested, in order:

1. Apply median filter to the original ROI with a square kernel of size 5.
2. Apply histogram equalization.
3. Apply gray-scale erosion to enhance dark areas
4. Apply a multilevel image thresholding, based on Otsu's method requesting 15 thresholds.
5. For each threshold obtain a binary image, followed by region labeling and compute various properties.

We followed until step 4 since computing 15 thresholds are computationally expensive and time-consuming, and impractical for a more extensive data set. Alternatively, we have used five thresholds. This should enable us to separate the mental foramen, given it is sufficiently visible. Then we pick the 2nd darkest threshold; the darkest will always be the black background. Hopefully, the MF will be the only or smallest segment in this binary image. Then, we easily obtain the contours in this image, select the largest one, and fit a bounding box around it.

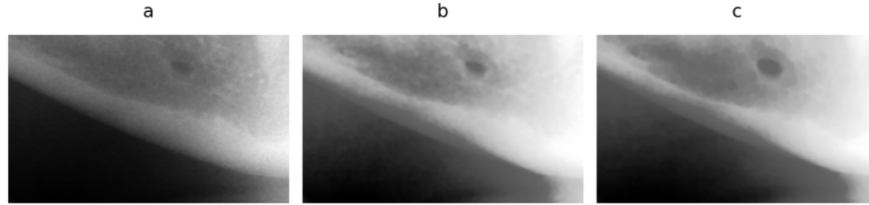


Figure 9: Figure column (a) shows the ROI, column (b) shows (a) after histogram equalization, column (c) shows (b) after gray-scale erosion.

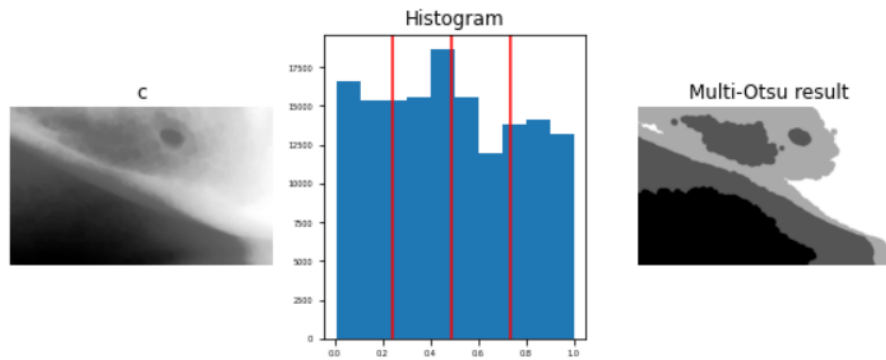


Figure 10: Figure column (c) the shows the gray-scale eroded image, then we see the histogram with three obtain thresholds. Far-right, the thresholded image is observed.

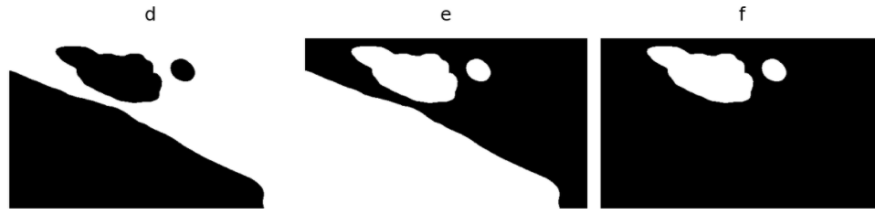


Figure 11: Figure column (d) shows the binary image obtained from threshold two, column (e) shows the (d) inverted, column (f) shows (d) after regions meeting the border has been removed.

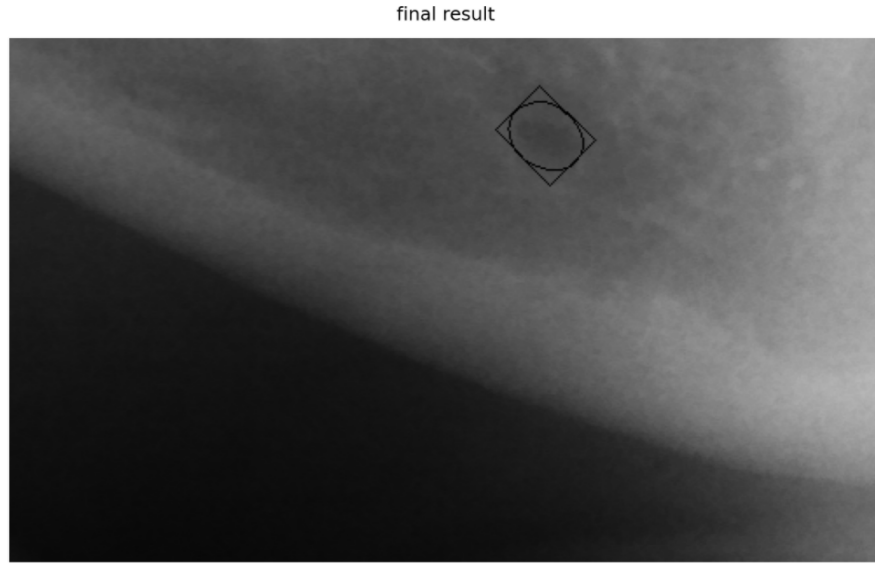


Figure 12: The figure shows the resulting contour and bounding box around the smallest region from figure 11f.

The problem with this technique is that it does not scale well. The reason is that the MF, most often, is not distinct; therefore, the threshold will cover both the MF and its surrounding area. Another common obstacle is that the wrong region is detected.

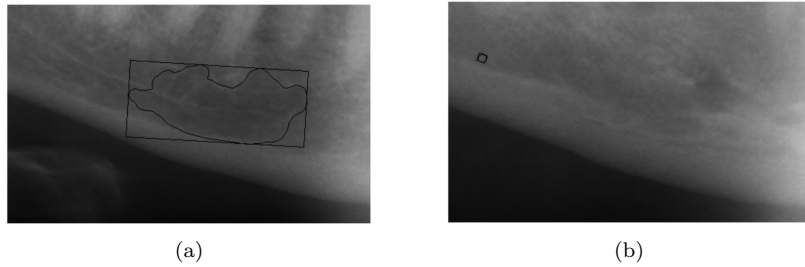


Figure 13: The figure presents two situations where the proposed method disappoints.

Another option is to try blob detection as the MF's intensity level is about constant. In this work, we do the following

1. Apply a median filter with kernel size 7 to the original.

2. Apply Otsu's method to obtain a binary mask (threshold) that separates the background from the foreground. Multiply the mask with the median filtered image to remove the background.
3. Follow with histogram equalization, and obtain the inverse image, so the MF is white rather than black making it easier to distinguish for the human eye.
4. Define various parameters for blobs to be detected; color, minimum circularity, minimum convexity, maximum and minimum area.
5. Apply blob-finding algorithm.

The reason behind step 2 is that we do not want to detect blobs inside artifacts. The various parameters are found by experimentation. The color parameter is set to detect white regions, and the minimum circularity is set to 0.3. Minimum convexity is set to 0.4, and the maximum and minimum area is set to 500 and 20, respectfully.

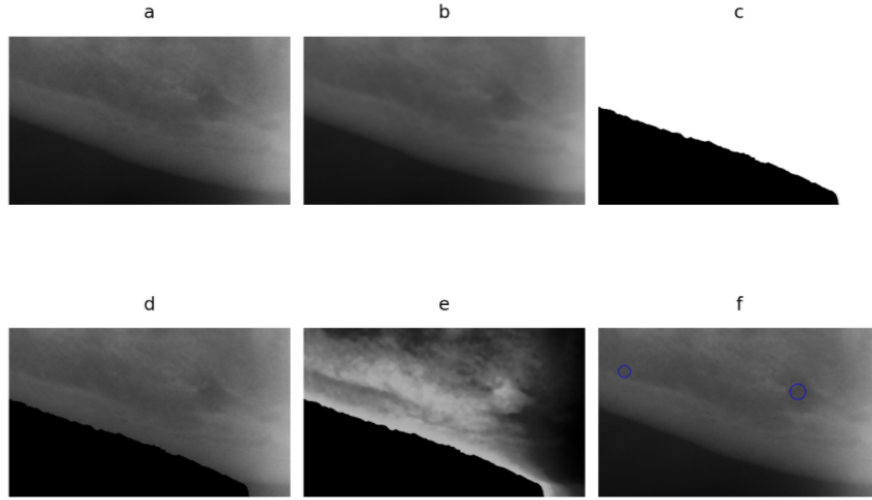


Figure 14: Image (a) shows the ROI, image (b) shows (a) after a median filter is applied, and image (c) shows a binary mask obtained from Otsu's method, image (d) shows image (b) multiplied with (c), image (e) shows (d) inverted, exposing the MF, image (f) shows the output after blob detection.

The figure above (14) shows that blob detection manages to find the MF where the previous method disappointed (figure 13 b). However, we see that the wrong region also has been recognized, forcing us to decide which one to use. This is unfortunate if several blobs are detected, which seems to be the typical case. Since both methods have significant issues, we cant employ them

without supervision. Therefore, we continue trying to measure the bone without the discovery of the MF. Meaning we have to choose the appropriate place to measure ourselves.

4.2 Measuring the bone

Again, two methods have been tested for measuring the width of the bone. First, we have adapted the method proposed by Aliaga et al. [23] to fit our images; second, we will try a different method using image enhancing techniques and the hybrid hessian filter. Aliaga et al. suggested, in order

1. Select a region of interest, compute a local variance image (texture description) on an 8-neighbourhood for each pixel.
2. Follow by global histogram equalization, obtaining an image I_v .
3. Apply a mean filter to image I_v with kernel set to 11, obtaining image I_m
4. Calculate the binary image I_b

$$I_b = \begin{cases} 1, & \text{if } I_m - I_v \geq s_t \\ 0, & \text{otherwise} \end{cases}$$

where s_t is the standard deviation of I_v

Here, we follow the same approach with minor adjustments. First, a median filter with kernel size set to 11 is applied to the ROI before computing the variance image. Here, the variance is computed on an 8-neighborhood also; then, global histogram equalization is applied, obtaining image I_v . After utilizing histogram equalization, obtaining image I_m , we employ a uniform filter with kernel size also set to 11. We compute the binary image in a different way

$$I_b = \begin{cases} 1, & \text{if } I_m - I_v \leq \sigma^2 \\ 0, & \text{otherwise} \end{cases}$$

where σ^2 is the variance of I_v . While no formal definition of texture exists, intuitively, such descriptors measure properties as smoothness, coarseness, grainy, and regularity. The variance is significant in texture description. It is a measure of intensity contrast that can further build descriptors of relative intensity smoothness [16]. Here we are interested in examining how homogeneous the jaw bone is. Implementing what we stated yield the results seen in figure 15.

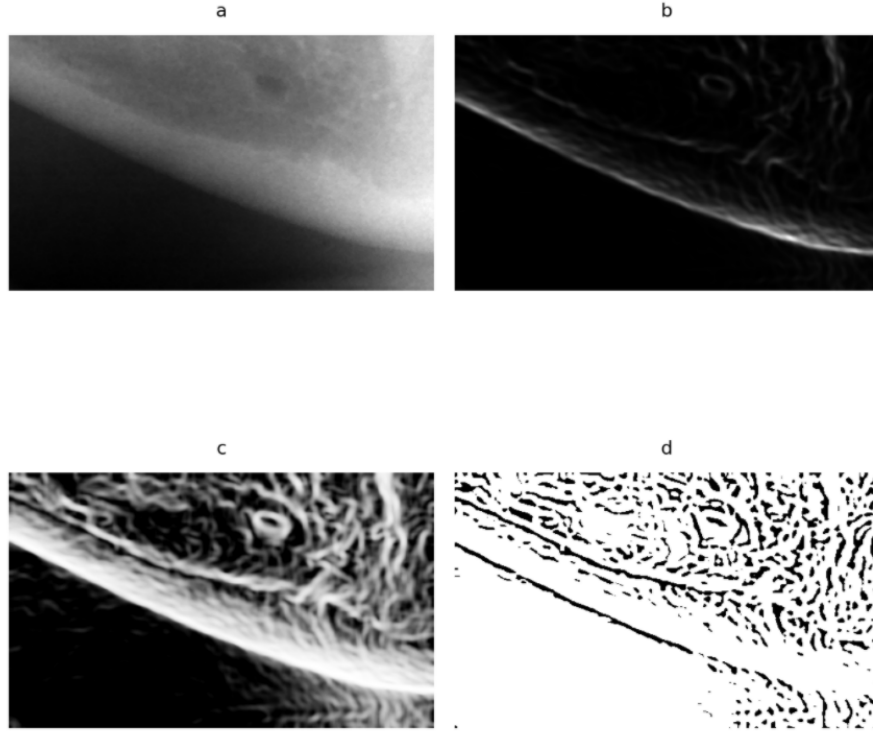


Figure 15: Image (a) displays the ROI, image (b) shows the variance image obtained after (a) is filtered with a median filter, image (c) shows (b) after histogram equalization, and image (d) shows the binary image I_b .

A key observation is that the bone appears almost entirely white but with dark spots along the upper edges, becoming more prominent further left in the bone. The ghost image from the spine partly causes the dark spots seen to the far left, but that is not too worrying as we are interested in the region below the MF. In this region, the spots are connected with the porosity of the bone. In figure 16 below, one can see three different cases of deterioration of the bone.

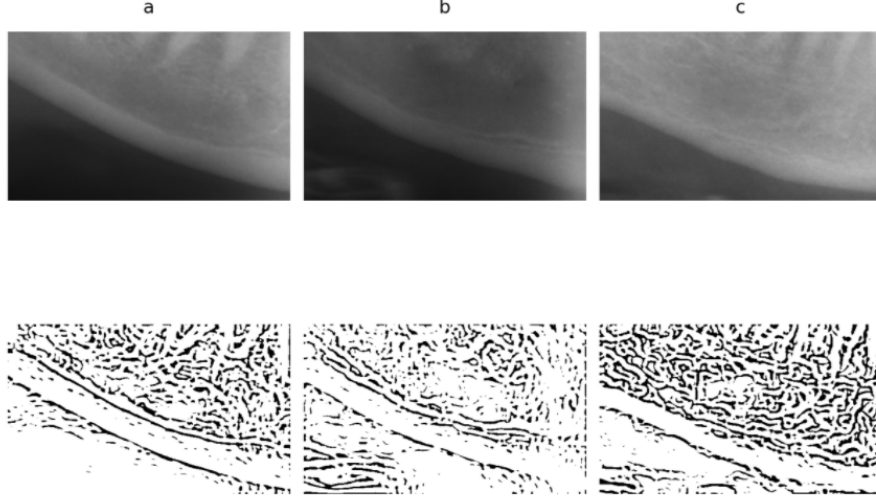


Figure 16: Figure column (a) shows an image and the resulting binary image of a Klemmti index C1, in the same manner (b) shows a case of C2, and column (c) displays a state of C3.

Before any measurements can be made, the lower boundary of the bone must be established. To do so, we further embrace the work done by Aliaga et al. Therefore, we apply a gray-scale dilation with a disk structure element of size 7 to all positive values, causing bright/dark areas to be emphasized. The dilation is applied to the variance image computed over a neighborhood of 5 pixels. The variance image is computed after employing a median filter with size 11 to the ROI. After gray-scale dilation, we employ multilevel image thresholding, based on Otsu, again, but we are requesting simply three thresholds.

A binary image is obtained with the three regions corresponding to pixels above the matching threshold, i.e., all pixels are set to binary values of 0, 1, or 2. We follow up with region labeling, and compute the following properties for each labeled region: area, major and minor axis length. Candidate regions should contain a relevant number of pixels, and therefore first select regions with an area greater than 4% of the total ROI area (6000 pixels). Which leads to small areas like teeth and blobs are discarded. Major and minor axis lengths are associated with an ellipse, so imagine an ellipse was fitted to every region. We choose those with major and minor axis lengths greater than 350 and 30 pixels, respectfully. One could go further and calculate the orientation and other properties of the regions, but what we have announced now is satisfactory.

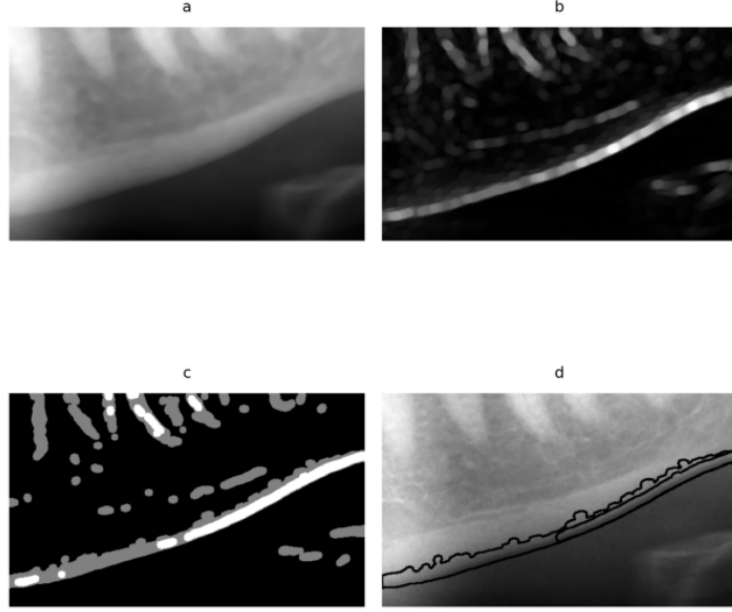


Figure 17: Image (a) displays the median filtered ROI, image (b) shows the result of gray-scale dilation applied to the variance image of (a), (c) presents the binary image with three thresholds, image (d) shows the contour of the candidate region after region labeling.

From figure 17 d, we see the contour from the candidate region. The upper left corner of the ROI is the origin of the coordinates, with the y-axis down and the x-axis pointing right. Selecting points with the maximum y-value of the y-coordinate obtains the lowest line of the contour, which is the input for the Hough [24, 25], transform [16]. To convert the Hough parameters (ρ, θ) to the parameter space (slope, intercept) of the image, we use

$$m = -\frac{\cos\theta}{\sin\theta}, \quad d = \frac{\rho}{\sin\theta} \quad (33)$$

where m is the slope of the straight line and d is the intercept. When several lines are identified in the Hough polar space, which determines several m and d parameters associated with the lines, we must pick the most promising line regarding its objective (tangent to the bone below the MF).

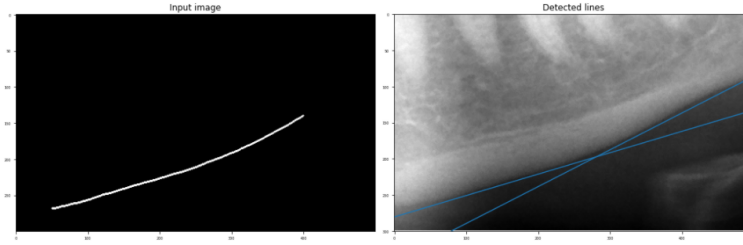


Figure 18: Here we see the input line, which is a part of the lowest contour of the candidate region, and the resulting lines after classical Hough transform.

After picking the best line, we select a segment consisting of 100 points, e.g., a segment from $x = 50$ to $x = 150$. Placing this segment on the binary image, we are set for the following scheme:

1. place the initial line on the binary image as shown in 15d
2. Calculate the percentage of white pixels the line overlap
3. Set a percentage threshold of 0.5
4. Move the line upwards by decreasing the intercept value (y-axis points down) until the threshold is met, resulting in a new line
5. Calculate the distance between the parallel lines (initial and final)

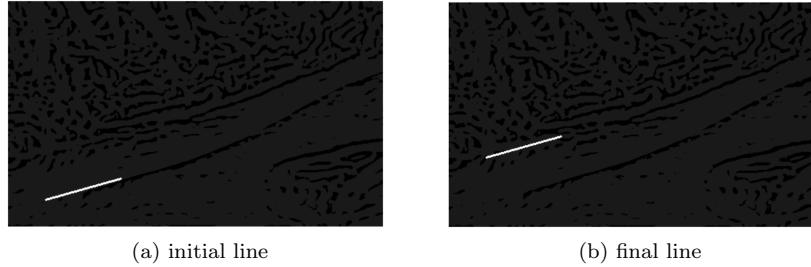


Figure 19: The figure displays an example of the initial and final state of the scheme.

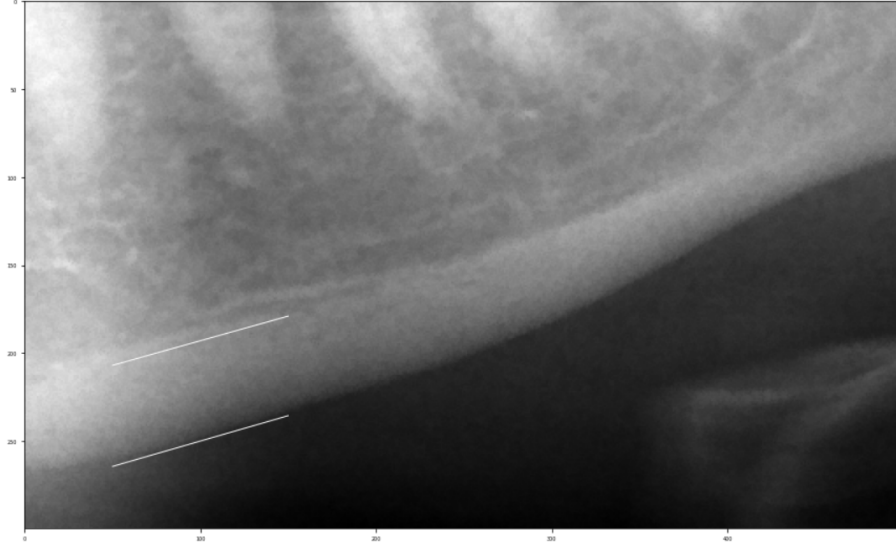


Figure 20: The figure displays both the initial and final line from which we measure the mandibular cortical width.

Figure 20 shows a promising result of the stated scheme. The method is somewhat extensive and requires many computations. Nevertheless, it does an excellent job from the looks of it. We will try another surprisingly simple method to measure the bone.

We have previously stated that the hybrid hessian filter (HHF) can detect ridge-like structures like veins and rivers. The bone can be regarded as a river in this context, and hence we will test the HHF as well. To do this, we apply the HHF to a blurred ROI then morphological operations to create a binary mask of the bone. When this is achieved, a contour and bounding box can easily be obtained. As the lowest edge of the bounding box will be tangent to the bone, a point corresponding to the MF must be determined. A line perpendicular to the tangent line drawn from our point will be used to measure the width of the bone.

Results after utilizing the HHF is seen in figure (21).

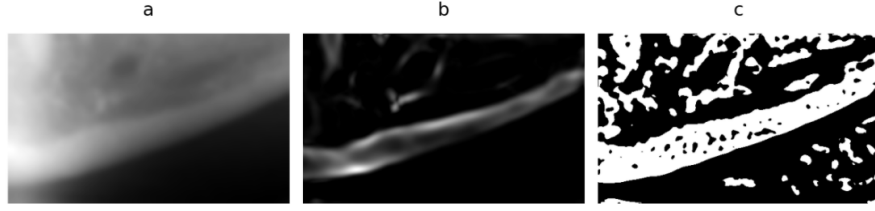


Figure 21: Figure image (a) displays ROI exposed to a Gaussian blur with kernel size 5, image (b) shows the Frangi filter response of image (a), image (c) shows the HHF response of image (a).

Filling the small openings in the binary image from figure (21c), finding the contour, and preserving the bounded regions results in a binary mask of the bone seen in figure (22).

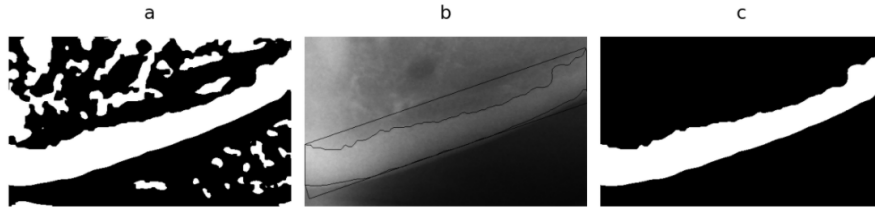


Figure 22: Figure image (a) displays a binary mask after a closing operation is applied to figure (21c), image (b) shows the most prominent contour and associated bounding box found in the image (a), image (c) shows a binary mask of the region bounded by the contour.

Using the image seen in (22c) and drawing a line between an appropriate point perpendicular to the bounding box, we can count the number of pixels on the line overlapping the binary mask and calculate the bone width.

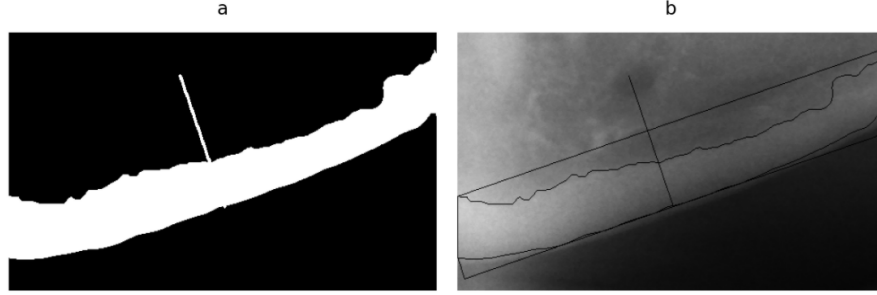


Figure 23: Image (a) shows a suitable line overlapping the binary mask, whereas (b) shows the same composition in the non-binary setting.

4.3 Results and discussion

The results of the measurements can be found in the appendix in table (4). Table (1) shows the correlation of inter-observer reliability for the mean mandibular cortical width for the experts and our experiments. Note that the correlation between the two experts is 0.908%, although this value is high, it cannot be regarded as "ground truth". In addition, we observe that algorithm 1 from the first experiment has a much higher correlation with both experts than algorithm 2 from the second experiment, which included the HHF. Due to the stopping criteria (threshold set at 50% "porosity"), the first experiment was more successful than the second. The latter failed to recognize the appropriate edge of the bone and overextended. In addition, it failed several times to identify the bone without including the ghost image of the spine, therefore, it was not sufficiently robust. It is important to keep in mind that both schemes might not measure at the correct location, since the mental foramen was not identified. Nevertheless, the first scheme involved measuring between lines wider than the mental foramen, thus making it more likely that it had taken place at the correct location. While we cannot be certain which method is more precise, even though this can be inferred from a correlation table, we can infer from the practice of utilizing these two methods that method 1 was more effective.

Table 1: Interobserver reliability for mean MCW

Inter-Item Correlation Matrix				
	Mean Algo 1	Mean Algo 2	Mean Expert 1	Mean Expert 2
Mean Algo 1	1.000	.378	.922	.956
Mean Algo 2	.378	1.000	.370	.483

Mean Expert 1	.922	.370	1.000	.908
Mean Expert 2	.956	.483	.908	1.000

Table 2: Statistics for algo 1

Intraclass Correlation Coefficient							
	Intraclass Correlation ^b	95% Confidence Interval		F-Test with True value 0			
		Lower Bound	Upper Bound	Value	df1	df2	Sig
Single Measures	0.875 ^a	0.772	0.931	28.197	45	90	0.000
Average Measures	0.955 ^c	0.910	0.976	28.197	45	90	0.000

Two-way mixed effects model where people effects are random and measures effects are fixed.

- a. The estimator is the same, whether the interaction effect is present or not.
- b. Type A intraclass correlation coefficients using an absolute agreement definition.
- c. This estimate is computed assuming the interaction effect is absent, because it is not estimable otherwise.

Table 3: Statistics for algo 2

Intraclass Correlation Coefficient							
	Intraclass Correlation ^b	95% Confidence Interval		F-Test with True value 0			
		Lower Bound	Upper Bound	Value	df1	df2	Sig
Single Measures	0.458 ^a	0.162	0.723	3.400	17	34	0.001
Average Measures	0.717 ^c	0.367	0.887	3.400	17	34	0.001

Two-way mixed effects model where people effects are random and measures effects are fixed.

- a. The estimator is the same, whether the interaction effect is present or not.
- b. Type A intraclass correlation coefficients using an absolute agreement definition.
- c. This estimate is computed assuming the interaction effect is absent, because it is not estimable otherwise.

4.4 Classification?

5 Concluding remarks

In this study, we have investigated the properties of the mental foramen and the jawbone in panoramic radiographs. As part of this process, we employed a range of spatial and algorithmic filters in order to generate a sense of how we could measure anatomical structures from radiographs. Due to the increasing sophistication and importance of medical images for diagnostic purposes, it is essential that we are aware of their characteristics and the pitfalls of working with them. For the position of the mental foramen, we experimented with two schemes, but unfortunately, our results were not satisfactory. Thus, we shifted our focus to measuring the bone. We conducted our experiment in two different ways and each yielded positive results. However, one of them proved to be more reliable than the other. Our efforts to produce this body of work have allowed us to gain an understanding of the inherent complexity of panoramic radiographs and the techniques required in order to overcome the associated obstacles. Additionally, we have a better understanding of the leading causes of variability in panoramic images. Beneficial methods for bone measurement have been observed, one of which being strong enough to overcome the challenge of an unclear bone edge. A dentist could benefit from this kind of knowledge as measuring anatomical structures is a time-consuming and challenging task. It is increasingly necessary and desirable to provide an automated system for handling such tasks, and we hope to further develop this methodology in the future.

5.1 Future work

We have gained a solid understanding of relevant image processing techniques through this project, and we have seen and experienced the challenges associated with radiograph analysis. It is intended that the next step in this work is to implement a fully automated measurement procedure. A task of this scope will not be trivial due to the complex nature of the radiographs. A possible option would be to have several schemes work together in order to find the best solution. Recent advances [26, 27, 28, 29] in machine learning have enabled artificial intelligence (AI) to perform impressively in complex data environments where humans are unable to identify high-dimensional relationships. An example of such a field is the field of osteoporosis, despite the technical and clinical challenges in applying machine learning methods. Consequently, using AI is also considered a viable option for achieving a completely automated process.

5.2 Appendix

Table 4: The table shows left and right measurements of the mandibular cortical width estimated by two experts and two algorithms. Absent results express that the width has not been measured. If the measurement was not successful, it's labeled as "no".

Left Expert 1	Right Expert 1	Left Expert 2	Right Expert 2	Left Algo 1	Right Algo 1	Left Algo 2	Right Algo 2
0.46	0.46	0.46	0.48	no	no	no	0.623
0.64	0.58	0.66	0.57	0.605	0.579	0.633	0.514
0.54	0.56	0.49	0.52	no	no	0.435	0.465
0.48	0.46	0.49	0.52	0.501	0.464	no	no
0.27	0.33	0.23	0.36	no	0.269	no	no
0.5	0.36	0.46	0.42	0.357	0.383	0.405	0.385
0.29	0.35	0.35	0.37	0.308	0.336	0.376	no
0.12	0.15	0.52	0.51	no	no	0.494	0.376
		0.36	0.39			no	0.395
0.48	0.53	0.59	0.53	0.455	0.532	0.494	no
0.16	0.29	0.37	0.39	0.256	0.318	no	no
0.38	0.28			no	0.25	0.474	0.277
0.24	0.37	0.29	0.4	0.28	0.421	no	0.524
no	no			no	no		
0.41	0.43	0.39	0.38	no	0.375	no	0.445
0.42	0.55	0.42	0.41	0.371	0.412	0.415	no
0.61	0.52	0.57	0.58	0.58	0.48	0.553	no
0.38	0.45	0.35	0.41	0.394	no	no	no
0.5	0.5	0.58	0.54	no	0.523	no	0.484
0.22	0.22	0.18	0.22	no	no	no	no
0.46	0.47	0.46	0.46	0.417	0.399	0.385	0.395
0.28	0.4	0.35	0.4	0.268	0.418	0.336	0.544
0.6	0.3	0.38	0.4	0.375	0.387	0.346	0.326
0.5	0.7	0.55	0.61	0.468	no	0.435	0.544
0.48	0.43	0.51	0.48	0.431	0.418	0.376	0.514

0.2	no	0.21	0.22	0.2	0.204	no	0.178
		0.13	no	no	no		
		0.19	0.16	0.23	0.166	0.168	0.37
0.38	0.3	0.3	0.36	0.334	0.3	no	no
0.47	0.45	0.42	0.41	0.474	0.384	no	no
		0.26	0.4	0.27	no	0.366	no
no	0.16	0.18	0.15	0.165	0.191	0.277	no
no	0.44	0.41	0.4	0.37	0.34	0.445	no
0.69	0.64	0.65	0.6	0.639	0.55	0.672	no
0.36	0.35	0.34	0.38	0.369	0.359	0.346	0.326
0.46	0.42	0.46	0.43	0.417	no	no	0.385
0.52	0.52	0.41	0.39	0.407	0.466	0.366	0.306
0.42	no	0.36	0.32	0.369	0.336	0.366	0.326
0.58	0.46	0.52	0.55	0.54	0.491	no	no
no	no					no	no
no	no					no	no
0.56	0.52	0.54	0.51	0.439	0.539	no	0.563
0.46	0.42	0.45	0.44	0.439	0.42	0.553	0.395
0.58	0.5	0.52	0.55	0.473	0.521	0.573	no
no	no	0.42	0.35	0.341	0.363	no	0.415
0.38	0.38			0.429	0.348	0.385	0.385
0.25	0.25	0.46	0.49	0.321	0.356	0.346	0.504
0.49	0.46	0.55	0.46	0.406	0.4	no	no
0.58	0.52	0.55	0.48	0.57	0.467	no	no
0.56	0.56	0.54	0.56	0.591	0.548	0.741	0.583
0.32	0.32	0.34	0.33	0.246	0.246	0.306	no
no	0.46	0.47	0.46	0.399	0.387	0.346	0.356
no	0.5	0.49	0.48	0.415	0.362	0.336	0.425
0.46	0.42	0.46	0.41	0.373	0.439	0.455	no
no	no			no	no	no	no
0.42	0.42	0.37	0.4	0.417	0.371	0.316	0.395

0.48	0.56			no	no	no	no
0.34	0.52	0.51	0.49	0.398	0.437	no	no
no	no			no	no	no	no
no	0.27	0.28	0.3	no	0.278	no	0.346
		0.44	0.48	0.498	no	no	no
		0.48	0.45	0.405	0.433	0.366	0.356
		0.5	0.59	no	0.44	no	no
		0.47	0.51	no	no	no	no
		0.51	0.48	no	0.456	0.366	0.405
		0.6	0.57	0.56	0.592	no	0.544
		0.54	0.55	no	0.52	no	no
		0.4	0.41	0.369	0.452	0.336	0.474
		0.41	0.36	0.389	0.359	0.465	0.356
		0.34	0.39	0.316	0.36	0.326	no
		0.51	0.48	0.534	0.475	0.474	no
0.52	0.41	0.46	0.47	0.399	0.307	0.573	0.474
		0.4	0.44	0.355	0.387	no	0.494
		0.42	0.4	0.395	0.35	no	0.356
		0.36	0.35	0.306	no	no	no
		0.42	0.47	0.406	0.416	0.425	no
0.19	0.25	0.19	0.23	0.186	0.186	no	no
0.41	0.47	0.45	0.42	0.45	0.441	no	no
		0.4	0.45	0.41	no	0.405	0.356
0.41	0.48	0.42	0.52	no	no	0.385	no
		0.38	0.44	0.329	0.39	0.474	no
		0.52	0.51	0.498	0.463	no	0.376
		0.59	0.49	0.55	0.49	0.435	0.504
		0.38	0.38	0.383	0.356	0.405	0.356
		0.58	0.52	no	0.46	no	0.553
		0.38	0.24	0.414	0.174	no	no
		0.4	0.47	0.364	0.46	0.326	0.336

		0.59	0.61	0.62	0.488	0.623	0.534
		0.18	0.22	0.252	0.249	0.376	0.385
		0.5	0.51	0.495	0.488	0.455	no
		0.47	0.4	0.431	0.382	0.376	0.316
		0.52	0.39	0.475	0.35	0.524	0.356
		0.35	0.36	no	0.344	no	no
		0.4	0.46	0.485	0.422	0.514	no
		0.59	0.52	0.536	0.514	no	no
		0.46	0.53	no	no	no	0.267
		0.5	0.47	0.446	0.446	0.376	no
		0.45	0.37	0.404	0.331	0.395	0.287
		0.41	0.38	0.403	0.394	no	0.484
		0.41	0.38	no	no	no	no
		0.57	0.53	no	0.351	0.346	no
		0.56	0.57	0.472	0.492	0.474	0.435
		0.48	0.59	0.46	0.532	no	no
		0.62	0.56	0.57	0.572	0.573	0.593
		0.61	0.54	0.538	0.539	no	0.474
		0.5	0.57	0.427	0.529	0.425	no
		0.57	0.62	no	no	no	no
		0.56	0.51	0.484	0.409	0.455	no
		0.55	0.57	0.557	0.468	0.563	0.455
		0.48	0.49	0.479	0.427	no	0.405
		0.61	0.55	0.462	0.378	0.39	0.395
		0.58	0.67	0.579	0.627	0.504	0.593
		0.58	0.62	no	0.63	no	no

References

- [1] E Calciolari, N Donos, JC Park, A Petrie, and N Mardas. Panoramic measures for oral bone mass in detecting osteoporosis: a systematic review and meta-analysis. *Journal of dental research*, 94(3_suppl):17S–27S, 2015.
- [2] SC White. Oral radiographic predictors of osteoporosis. *Dentomaxillofacial radiology*, 31(2):84–92, 2002.
- [3] About Osteoporosis | International Osteoporosis Foundation.
- [4] World Health Organization et al. Who scientific group on the assessment of osteoporosis at primary health care level. In *Summary meeting report*, volume 5, pages 5–7, 2004.
- [5] K. Horner and H. Devlin. The relationship between mandibular bone mineral density and panoramic radiographic measurements. *Journal of Dentistry*, 26(4):337–343, May 1998.
- [6] B. W. Benson, T. J. Prihoda, and B. J. Glass. Variations in adult cortical bone mass as measured by a panoramic mandibular index. *Oral Surgery, Oral Medicine, and Oral Pathology*, 71(3):349–356, March 1991.
- [7] E. Klemetti, S. Kolmakov, and H. Kröger. Pantomography in assessment of the osteoporosis risk group. *Scandinavian Journal of Dental Research*, 102(1):68–72, February 1994.
- [8] Akira Taguchi, Yoshikazu Suei, Mitsuhiro Sanada, Masahiko Ohtsuka, Takashi Nakamoto, Hiroomi Sumida, Koso Ohama, and Keiji Tanimoto. Validation of dental panoramic radiography measures for identifying postmenopausal women with spinal osteoporosis. *American journal of roentgenology*, 183(6):1755–1760, 2004.
- [9] Akira Taguchi, Mitsuhiro Sanada, Elizabeth Krall, Takashi Nakamoto, Masahiko Ohtsuka, Yoshikazu Suei, Keiji Tanimoto, Ichiro Kodama, Mikio Tsuda, and Koso Ohama. Relationship between dental panoramic radiographic findings and biochemical markers of bone turnover. *Journal of Bone and Mineral Research*, 18(9):1689–1694, 2003.
- [10] Takashi Nakamoto, Akira Taguchi, Masahiko Ohtsuka, Yoshikazu Suei, Minoru Fujita, Keiji Tanimoto, Mikio Tsuda, Mitsuhiro Sanada, Koso Ohama, Junichiro Takahashi, et al. Dental panoramic radiograph as a tool to detect postmenopausal women with low bone mineral density: untrained general dental practitioners’ diagnostic performance. *Osteoporosis international*, 14(8):659–664, 2003.
- [11] Anne-Marie Bollen, Akira Taguchi, Philippe P Hujoel, and Lars G Hollender. Case-control study on self-reported osteoporotic fractures and mandibular cortical bone. *Oral Surgery, Oral Medicine, Oral Pathology, Oral Radiology, and Endodontology*, 90(4):518–524, 2000.

- [12] A Taguchi, Y Suei, M Ohtsuka, K Otani, K Tanimoto, and M Ohtaki. Usefulness of panoramic radiography in the diagnosis of postmenopausal osteoporosis in women. width and morphology of inferior cortex of the mandible. *Dentomaxillofacial Radiology*, 25(5):263–267, 1996.
- [13] Akira Taguchi, Masahiko Ohtsuka, Mikio Tsuda, Takashi Nakamoto, Ichiro Kodama, Koji Inagaki, Toshihide Noguchi, Yoshiki Kudo, Yoshikazu Suei, and Keiji Tanimoto. Risk of vertebral osteoporosis in post-menopausal women with alterations of the mandible. *Dentomaxillofacial Radiology*, 36(3):143–148, 2007.
- [14] Tabinda Hasan. Morphology of the mental foramen;a must know in clinical dentistry. *journal of Pakistan Dental Association*, 21:167–172, January 2012.
- [15] H. Devlin and J. Yuan. Object position and image magnification in dental panoramic radiography: a theoretical analysis. *Dentomaxillofacial Radiology*, February 2014. Publisher: The British Institute of Radiology. 131–151 Great Titchfield Street, London W1W 5BB.
- [16] Rafael C Gonzalez. Richard e. woods digital image processing, pearson, 2018.
- [17] Irwin Sobel and Gary Feldman. A 3x3 isotropic gradient operator for image processing. *a talk at the Stanford Artificial Project in*, pages 271–272, 1968.
- [18] Alejandro F Frangi. *Three-dimensional model-based analysis of vascular and cardiac images*. PhD thesis, 2001.
- [19] Michal Sofka and Charles V Stewart. Retinal vessel centerline extraction using multiscale matched filters, confidence and edge measures. *IEEE transactions on medical imaging*, 25(12):1531–1546, 2006.
- [20] M Elena Martinez-Perez, Alun D Hughes, Simon A Thom, Anil A Bharath, and Kim H Parker. Segmentation of blood vessels from red-free and fluorescein retinal images. *Medical image analysis*, 11(1):47–61, 2007.
- [21] Choon-Ching Ng, Moi Hoon Yap, Nicholas Costen, and Baihua Li. Automatic Wrinkle Detection Using Hybrid Hessian Filter. In Daniel Cremers, Ian Reid, Hideo Saito, and Ming-Hsuan Yang, editors, *Computer Vision – ACCV 2014*, Lecture Notes in Computer Science, pages 609–622, Cham, 2015. Springer International Publishing.
- [22] Alejandro F Frangi, Wiro J Niessen, Koen L Vincken, and Max A Viergever. Multiscale vessel enhancement filtering. In *International conference on medical image computing and computer-assisted intervention*, pages 130–137. Springer, 1998.

- [23] Ignacio Aliaga, Vicente Vera, María Vera, Enrique García, María Pedrera, and Gonzalo Pajares. Automatic computation of mandibular indices in dental panoramic radiographs for early osteoporosis detection. *Artificial Intelligence in Medicine*, 103:101816, March 2020.
- [24] Paul VC Hough. Method and means for recognizing complex patterns, December 18 1962. US Patent 3,069,654.
- [25] E Roy Davies. *Computer vision: principles, algorithms, applications, learning*. Academic Press, 2017.
- [26] Mandibular Radiomorphometric Indices and Tooth Loss as Predictors for the Risk of Osteoporosis using Panoramic Radiographs. *Oral Health and Preventive Dentistry*, 18(1):773–782, February 2020.
- [27] Ki-Sun Lee, Seok-Ki Jung, Jae-Jun Ryu, Sang-Wan Shin, and Jinwook Choi. Evaluation of Transfer Learning with Deep Convolutional Neural Networks for Screening Osteoporosis in Dental Panoramic Radiographs. *Journal of Clinical Medicine*, 9(2):392, February 2020. Number: 2 Publisher: Multidisciplinary Digital Publishing Institute.
- [28] Chirath Dasanayaka, Bhasitha Dharmasena, Wikum Roshan Bandara, Maheshi Buddhinee Dissanayake, and R Jayasinghe. Segmentation of Mental Foramen in Dental Panoramic Tomography using Deep Learning. In *2019 14th Conference on Industrial and Information Systems (ICIIS)*, pages 81–84, December 2019. ISSN: 2164-7011.
- [29] Jae-Seo Lee, Shyam Adhikari, Liu Liu, Ho-Gul Jeong, Hyongsuk Kim, and Suk-Ja Yoon. Osteoporosis detection in panoramic radiographs using a deep convolutional neural network-based computer-assisted diagnosis system: a preliminary study. *Dentomaxillofacial Radiology*, 48(1):20170344, 2019.